



**Observed Flow Compensation Associated with the
MOC at 26.5°N in the Atlantic**

Torsten Kanzow, *et al.*
Science **317**, 938 (2007);
DOI: 10.1126/science.1141293

**The following resources related to this article are available online at
www.sciencemag.org (this information is current as of August 17, 2007):**

Updated information and services, including high-resolution figures, can be found in the online version of this article at:

<http://www.sciencemag.org/cgi/content/full/317/5840/938>

Supporting Online Material can be found at:

<http://www.sciencemag.org/cgi/content/full/317/5840/938/DC1>

This article **cites 20 articles**, 2 of which can be accessed for free:

<http://www.sciencemag.org/cgi/content/full/317/5840/938#otherarticles>

This article has been **cited by** 1 articles hosted by HighWire Press; see:

<http://www.sciencemag.org/cgi/content/full/317/5840/938#otherarticles>

This article appears in the following **subject collections**:

Oceanography

<http://www.sciencemag.org/cgi/collection/oceans>

Information about obtaining **reprints** of this article or about obtaining **permission to reproduce this article** in whole or in part can be found at:

<http://www.sciencemag.org/about/permissions.dtl>

Sea Systems mooring team. The mooring operations are funded by NERC and NSF. The Florida Current cable data are made freely available by the AOML (www.aoml.noaa.gov/phod/floridacurrent/) and are funded by the NOAA Office of Climate Observations. Wind stress data were obtained from the Centre for Satellite Exploitation and

Research, at the Institut français de recherche pour l'exploitation de la mer, Plouzané, France.

Figs. S1 to S4
References

Supporting Online Material

www.sciencemag.org/cgi/content/full/317/5840/935/DC1
SOM Text

14 February 2007; accepted 12 July 2007
10.1126/science.1141304

Observed Flow Compensation Associated with the MOC at 26.5°N in the Atlantic

Torsten Kanzow,^{1*} Stuart A. Cunningham,¹ Darren Rayner,¹ Joël J.-M. Hirschi,¹ William E. Johns,² Molly O. Baringer,³ Harry L. Bryden,¹ Lisa M. Beal,² Christopher S. Meinen,³ Jochem Marotzke^{4*}

The Atlantic meridional overturning circulation (MOC), which provides one-quarter of the global meridional heat transport, is composed of a number of separate flow components. How changes in the strength of each of those components may affect that of the others has been unclear because of a lack of adequate data. We continuously observed the MOC at 26.5°N for 1 year using end-point measurements of density, bottom pressure, and ocean currents; cable measurements across the Straits of Florida; and wind stress. The different transport components largely compensate for each other, thus confirming the validity of our monitoring approach. The MOC varied over the period of observation by $\pm 5.7 \times 10^6$ cubic meters per second, with density-inferred and wind-driven transports contributing equally to it. We find evidence for depth-independent compensation for the wind-driven surface flow.

The Atlantic meridional overturning circulation (MOC) consists of a near-surface, warm northward flow, compensated for by a southward return flow at depth. Heat loss to the atmosphere makes the increasingly dense northward-flowing surface waters sink at high latitudes to feed the deep return flow (*I*). The vertical temperature contrast associated with this flow results in a northward heat transport of 1.3×10^{15} W at 24°N (*2*), which noticeably moderates the Northeast Atlantic climate (*3, 4*).

Most of the observation-based estimates of Atlantic MOC strength are based on infrequently acquired zonal hydrographic sections. Because the frequency distribution of the MOC variability is unknown, long-term changes inferred from these snapshot sections (*5*) may not be representative. Basic MOC characteristics, such as magnitude and time scales of natural variability (*6*), response to local wind-stress forcing, or the relative importance of wind-stress and buoyancy forcing on subseasonal-to-decadal time scales (*7, 8*),

have not yet been observed. Our ability to detect future MOC changes depends on the accurate quantification of the MOC's spectral distribution and on understanding the physical processes involved.

We analyzed MOC variability on subseasonal time scales using a 1-year-long mooring-based volume-transport time series from March 2004 to March 2005, acquired in the framework of the rapid climate change/meridional overturning circulation and heat flux array (RAPID/MOCHA) experiment (*9, 10*). To compute the MOC, the zonally integrated meridional flow across 26.5°N as a function of depth (*z*) was observed. The backbones of this effort are moorings that measure full water-column profiles of density and ocean-bottom pressure at the western and eastern endpoints of the basin interior (Fig. 1) and on both sides of the Mid-Atlantic Ridge (MAR) (fig. S2). The eastern-to-western boundary-density difference allows for the computation of the temporal evolution of the basin-wide integrated geostrophic-transport profile relative to 4820 dbar

¹National Oceanography Centre, Empress Dock, Southampton, SO14 3ZH, UK. ²Rosenstiel School of Marine and Atmospheric Science, 4600 Rickenbacker Causeway, Miami, FL 33149, USA. ³National Oceanic and Atmospheric Administration Atlantic Oceanographic and Meteorological Laboratory, 4301 Rickenbacker Causeway, Miami, FL 33149, USA. ⁴Max-Planck-Institut für Meteorologie, Bundesstraße 53, 20146 Hamburg, Germany.

*To whom correspondence should be addressed. E-mail: tok@noc.soton.ac.uk (T.K.); jochem.marotzke@zmaw.de (J.M.)

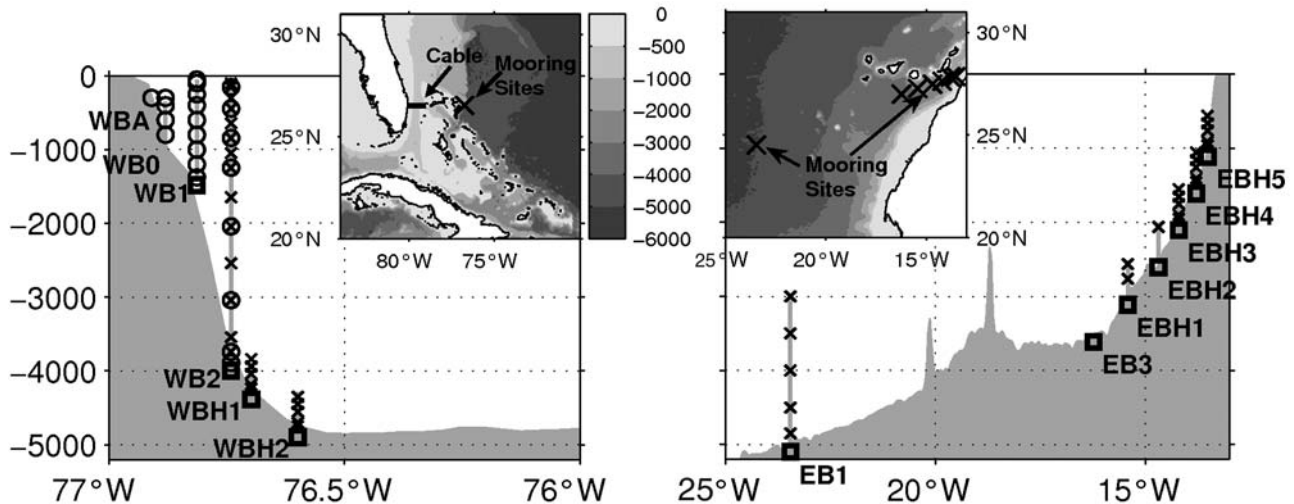


Fig. 1. Distribution of density (crosses) and bottom-pressure sensors (squares) of the RAPID/MOCHA moorings at the western and eastern boundaries of the subtropical North Atlantic near 26.5°N that are used for computing the zonally integrated meridional geostrophic flow. Direct current-meter measurements at the western boundary (circles)

complement the observations in the upper part of the western-boundary continental slope. The location of the western- and eastern-boundary mooring sites and that of the Straits of Florida telephone cable can be seen in the insets. WBA, western boundary acoustic doppler current profiler; WBH, western boundary homer; EB, eastern boundary.

(11, 12) [supporting online material (SOM)], referred to as internal transport (T_{INT}). We ignored the presence of the MAR in the calculations of the geostrophic flow; however, its effect is assessed crudely in the SOM. Zonal differences of bottom-pressure fluctuations between adjacent stations provide the temporally varying, zonally integrated reference-level contribution of the geostrophic flow (11, 12) (SOM), referred to as external transport (T_{EXT}). The meridional-transport profile over the continental slope west of mooring western boundary 1 (WB1) (Fig. 1, left)—hereafter referred to as western-boundary wedge transports (T_{WBW})—was estimated from direct current-meter measurements (SOM). Gulf Stream transports through the Straits of Florida (T_{GS}) are monitored by National Oceanic and Atmospheric Administration (NOAA) submarine cable measurements (13) (SOM). The coast-to-coast integrated wind-driven Ekman transports (T_{EK}), confined to a thin layer at the sea surface, are derived from spaceborne scatterometry (14) (SOM).

The sum of T_{EXT} (geostrophic reference-level contribution), T_{INT} (relative geostrophic contribution), and T_{WBW} yields the geostrophic mid-ocean transport fluctuations (T_{MO}) integrated across the transatlantic section, relative to a time-invariant offset (11, 15). Thus, when MOC variability is addressed, a time-variable flow adjust-

ment is not required, in contrast to traditional hydrographic-section data analyses where mass conservation is imposed to derive absolute transports (5, 16). This gives us two alternative approaches to compute MOC fluctuations from the transport per-unit-of-depth profiles: $T_{\text{INT}}(z) + T_{\text{EXT}}(z) + T_{\text{WBW}}(z) + T_{\text{EK}}(z) + T_{\text{GS}}(z)$ and the traditional $T_{\text{INT}}(z) + T_{\text{WBW}}(z) + T_{\text{EK}}(z) + T_{\text{GS}}(z) +$ mass-conservation constraint. Our observing system allows us to study: (i) the order of magnitude and time scales of MOC variability and (ii) how compensation of volume fluxes is distributed vertically and accomplished among the different transport components. As we show below, (ii) is a prerequisite for (i).

The fluctuations (time-mean-subtracted) of the vertically integrated profiles in Fig. 2A amounted to $\pm 8.3, 12.6, 1.1, 4.4,$ and 3.3 Sv (17, 18) for $\overline{T_{\text{INT}}}, \overline{T_{\text{EXT}}}, \overline{T_{\text{WBW}}}, \overline{T_{\text{EK}}},$ and $\overline{T_{\text{GS}}}$, respectively. (Overbars denote transport integrated vertically over the entire depth range.) Assuming that mass is conserved across a transatlantic section, one would expect the different transport contributions shown in Fig. 2A to compensate for each other. As a first indication, $\overline{T_{\text{INT}}}$ and $\overline{T_{\text{EXT}}}$ display negatively correlated fluctuations on monthly time scales. On the other hand, on daily to weekly time scales, none of the contributions can possibly compensate for the large

variability seen in $\overline{T_{\text{EXT}}}$ (± 8.0 Sv when applying a 10-day high-pass filter). Thus, in the high-frequency limit, zero net flow across the section is not a good approximation.

Because flow compensation for the different components occurs during periods longer than 10 days (fig. S1), we restricted the analysis to low frequencies by applying a 15-day low-pass filter to the transport components. After filtering, fluctuations amounted to $\pm 7.4, 9.1, 1.0, 3.9,$ and 3.1 Sv for $\overline{T_{\text{INT}}}, \overline{T_{\text{EXT}}}, \overline{T_{\text{WBW}}}, \overline{T_{\text{EK}}},$ and $\overline{T_{\text{GS}}}$, respectively. We observed a maximum negative correlation of -0.83 between $\overline{T_{\text{INT}}}$ and $\overline{T_{\text{EXT}}}$ at zero time lag. It appears plausible that random boundary-density fluctuations affecting $\overline{T_{\text{INT}}}$, primarily caused by Rossby waves impinging onto the western boundary (6) or by boundary waves propagating southward, act to create a mass imbalance, whereas $\overline{T_{\text{EXT}}}$, being composed of depth-invariant motions (SOM), responds quickly to maintain mass balance. $\overline{T_{\text{MO}}}$ and the sum of $\overline{T_{\text{EK}}}$ and $\overline{T_{\text{GS}}}$ (referred to as western and surface-boundary transport $\overline{T_{\text{BOUND}}}$) display a negative correlation of -0.74 (ignoring the period from September to October 2004 when $\overline{T_{\text{GS}}}$ was not measured) (Fig. 2B). The fact that $\overline{T_{\text{MO}}}$ and $\overline{T_{\text{BOUND}}}$ (being completely independent measurements) strongly compensate for each other demonstrates that our MOC observing strategy, using moorings at the section end points only to monitor $T_{\text{MO}}(z)$, is successful.

$\overline{T_{\text{GS}}}$ and $\overline{T_{\text{EK}}}$ are essentially uncorrelated (-0.04). However, compensation for both in equal shares is provided by $\overline{T_{\text{MO}}}$, with each showing a similar amount of negative correlation to $\overline{T_{\text{MO}}}$ (-0.47 for $\overline{T_{\text{GS}}}$ and -0.55 for $\overline{T_{\text{EK}}}$). $\overline{T_{\text{EK}}}$ displays a weak but significant negative correlation (19) to $\overline{T_{\text{EXT}}}$ (-0.32) and an insignificant correlation to $\overline{T_{\text{INT}}}$ (0.05). Thus, compensation for $\overline{T_{\text{EK}}}$ variability is primarily provided by $\overline{T_{\text{EXT}}}$. Because the 2-month gap in $\overline{T_{\text{BOUND}}}$ would have limited our analysis to 10 months, we filled the gap (Fig. 2B) by means of a linear regression between $\overline{T_{\text{MO}}}$ and $\overline{T_{\text{BOUND}}}$ (SOM).

There is a mass imbalance in the unconstrained total transport, defined as $\overline{T_{\text{MO}}} + \overline{T_{\text{BOUND}}}$ (Fig. 2B), although it amounts to only ± 3.4 Sv, compared to ± 4.9 Sv for $\overline{T_{\text{BOUND}}}$ (leaving out the period from September to October). Uncertainties of the five measurement components yielding ± 2.7 Sv (SOM) account for a substantial part of the imbalance. The remaining ± 2.1 Sv ($\sqrt{3.4^2 - 2.7^2}$ Sv) of the imbalance may arise from deficiencies, such as the flow below 4820 dbar not being included in $T_{\text{MO}}(z)$ and the role of the MAR in possibly upsetting the balance between the coast-to-coast integrated meridional flow and the coast-to-coast pressure gradient not being assessed. Observed transport fluctuations through the Bering Strait (20) suggest that an imbalance of ± 0.66 Sv across 26.5°N on intraannual time scales may exist.

We inferred MOC-transport variability from the vertical distribution of meridional-transport

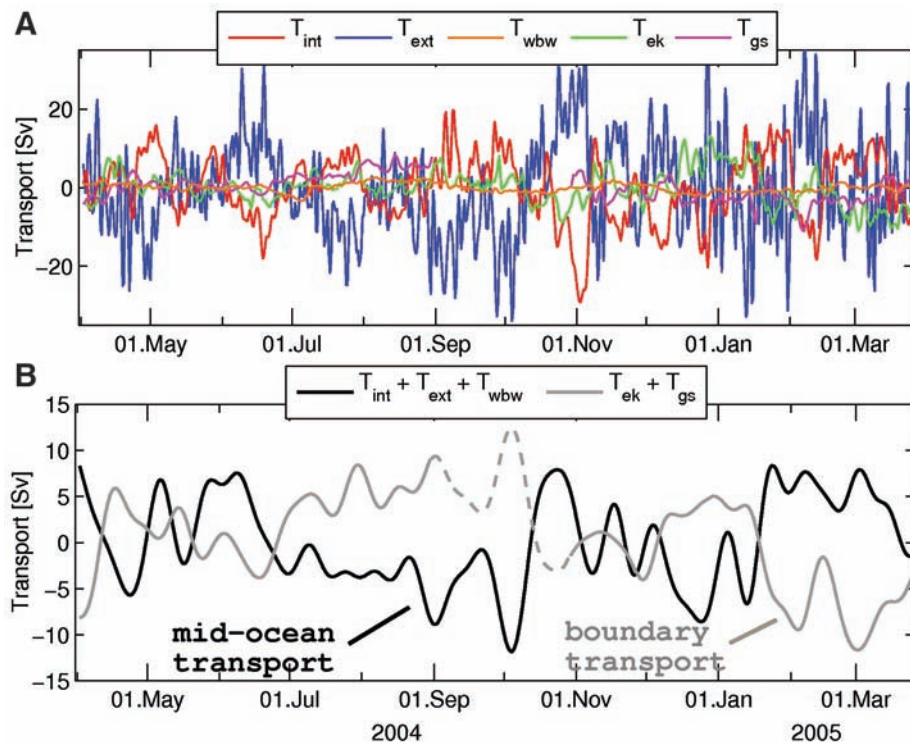


Fig. 2. (A) Fluctuations of $\overline{T_{\text{INT}}}$, red; $\overline{T_{\text{EXT}}}$, blue; $\overline{T_{\text{WBW}}}$, orange; $\overline{T_{\text{EK}}}$, green; and $\overline{T_{\text{GS}}}$, magenta (table S2). There is a 2-month gap in $\overline{T_{\text{GS}}}$ between 31 August and 29 September 2004. All time series were 2-day low-pass filtered and subsampled on a half-daily grid. The initial sampling rates were 15 min for the underlying density and current measurements and 10 min for the bottom pressure. (B) Fifteen-day low-pass-filtered fluctuations of vertically integrated mid-ocean transport ($\overline{T_{\text{MO}}} = \overline{T_{\text{INT}}} + \overline{T_{\text{EXT}}} + \overline{T_{\text{WBW}}}$) and boundary transports ($\overline{T_{\text{BOUND}}} = \overline{T_{\text{EK}}} + \overline{T_{\text{GS}}}$) as black and gray lines, respectively. The dashed part of the gray line denotes the period when $\overline{T_{\text{GS}}}$ could not be measured. A linear regression between $\overline{T_{\text{MO}}}$ and $\overline{T_{\text{BOUND}}}$ was used to fill this gap (SOM).

fluctuations. Over the 12-month period, the cumulative unconstrained total transport fluctuations (integrated upward from 4820 dbar toward the sea surface) show fluctuations of ± 3.9 Sv at 3600 dbar, have their peak value of ± 5.7 Sv at 1040 dbar and reduce to ± 3.0 Sv at the sea surface (Fig. 3). Given that we observed the maximum value near 1000 dbar, the transports integrated between 1000 and 4820 dbar will be referred to as MOC transports, following the traditional view that the MOC represents a two-layer flow. The small change in the cumulative transports at mid-depths (between 3600 and 1000 dbar) suggests that the MOC variability is dominated by near-bottom and upper-ocean contributions.

We computed the MOC variability using the traditional approach to infer MOC transports from hydrographic-section data (5, 16). Instead of using $T_{EXT}(z)$, we imposed an across-section zero-net-flow constraint at each time step by adding a depth-independent compensation. This allowed us (i) to estimate the relative importance of the density-inferred and locally wind-stress-driven contributions and (ii) to test the reliability of the traditional method by comparing it to the above unconstrained MOC estimate. To isolate the geostrophic contribution to the MOC, we assumed $T_{EK}(z)$ to be time-invariant. Thus, we constrained the vertical integral of $T_{INT}(z) + T_{WBW}(z) + T_{GS}(z)$ to be zero at each time step (Fig. 3, light blue line) and referred to it as constrained total geostrophic transport, assuming $T_{WBW}(z)$ and $T_{GS}(z)$ to be largely in geostrophic balance. This MOC-transport contribution neglecting $T_{EK}(z)$ varies by ± 4.1 Sv, peaking at 1160 dbar.

The constrained total transport [zero-net-flow constraint imposed on $T_{INT}(z) + T_{WBW}(z) + T_{EK}(z) + T_{GS}(z)$] displays an Ekman-induced strong increase in near-surface variability (Fig. 3, orange line) with a maximum value of ± 4.8 Sv at 920 dbar. This amplitude and the gradual increase below the Ekman layer are similar to the unconstrained total transport. However, with only ± 2.3 Sv at 3600 dbar, the cumulative constrained total transport shows a nearly uniform (rather than depth-intensified) increase between the bottom and the depth of maximum variability, as compared with the unconstrained transport. The fact that the peak-level amplitude of the constrained total flow is slightly less than that of the unconstrained total flow can partly be explained by having considered only the baroclinic flow between WB1 and WB2 in the constrained solution to simulate the traditional approach of inferring MOC transports (SOM).

For each of the cases, MOC-transport time series are computed (Fig. 4). The unconstrained MOC fluctuations (Fig. 4, black line) cover a range of 28.3 Sv. For the constrained total geostrophic (Fig. 4, light blue line) and total (Fig. 4, orange line) MOC contributions, the ranges are 21.8 and 24.7 Sv, respectively. The correlations between the unconstrained total MOC transport and the constrained total geo-

strophic and total MOC transport yield 0.60 and 0.82, respectively. Not only do the overall magnitudes of the unconstrained and constrained total transport variability agree (Fig. 4, black and orange lines), but their temporal evolutions are similar, too. Thus, deriving MOC variability from constrained flows [computed from continuous observations of $T_{INT}(z)$, $T_{WBW}(z)$, $T_{EK}(z)$, and $T_{GS}(z)$] appears to be a reliable technique for periods longer than 15 days. Also, as noted earlier, $\overline{T_{EXT}}$ shows a weak negative correlation to $\overline{T_{EK}}$. When including $T_{EK}(z)$ into the constrained solution [which excludes $T_{EXT}(z)$], the correlation between the resulting MOC transport and that from the unconstrained solution [which uses $T_{EXT}(z)$] increases. We therefore conclude that the depth-independent compensation for $T_{EK}(z)$ is partly contained in $\overline{T_{EXT}}$ (7).

In conclusion, the section-wide integrated $T_{MO}(z)$ and $T_{BOUND}(z)$ largely compensate for each other. This is strong evidence that the endpoint mooring approach to continuously monitor the MOC is valid. A net flow imbalance of ± 3.4 Sv remains, which is mainly attributable to measurement errors of ± 2.7 Sv. However, a time-variable transport imbalance of ± 0.66 Sv may actually exist, associated with Bering Strait throughflow (20). The measurement uncertainty

in MOC fluctuations should amount to only ± 2.0 Sv and consequently be smaller than the top-to-bottom integrated ± 3.4 -Sv imbalance, because only the flow deeper than 1000 dbar needs to be considered (SOM).

During periods shorter than 10 days, fluctuations of ± 8.0 Sv in T_{EXT} remain uncompensated for. Recent evidence from $\overline{T_{EXT}}$ observed in an experiment at 16°N indicates that the high-frequency fluctuations exhibit spatial correlation scales of more than 1000 km (21). For the high-frequency flow to be unbalanced would require the average water-column height of the North Atlantic to fluctuate coherently by ± 2 to 3 cm during periods < 10 days for which indications have been found (22, 23).

At 26.5°N, much of the observed compensation of the (zonally integrated) flows is expected to take place close to the western boundary (24); however, this may not hold at other latitudes (11, 25).

Both the unconstrained and constrained total transports display maximum cumulative variability (from the bottom up to 1000 dbar) of ± 5.7 and ± 4.8 Sv, respectively, with the former showing near-bottom intensified variability resulting from zonally non-uniform contributions in $T_{EXT}(z)$ over variable topography (which the

Fig. 3. Standard deviation of cumulative-transport fluctuations integrated upward from 4820 dbar. The black line shows the cumulative total unconstrained transports [$T_{INT}(z) + T_{EXT}(z) + T_{WBW}(z) + T_{EK}(z) + T_{GS}(z)$]. For the remaining two curves, a constraint of zero net flow across the 26.5°N section was imposed at each time step. The cumulative constrained total geostrophic [$T_{INT}(z) + T_{WBW}(z) + T_{GS}(z)$] and constrained total [$T_{INT}(z) + T_{WBW}(z) + T_{EK}(z) + T_{GS}(z)$] transport fluctuations are displayed as light blue and orange lines, respectively (table S3). All time series were 15-day low-pass filtered.

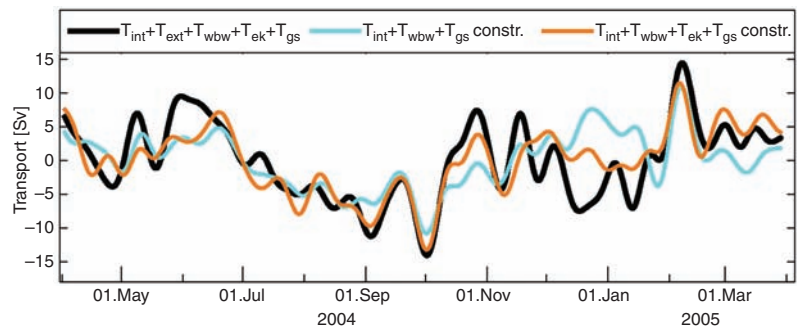
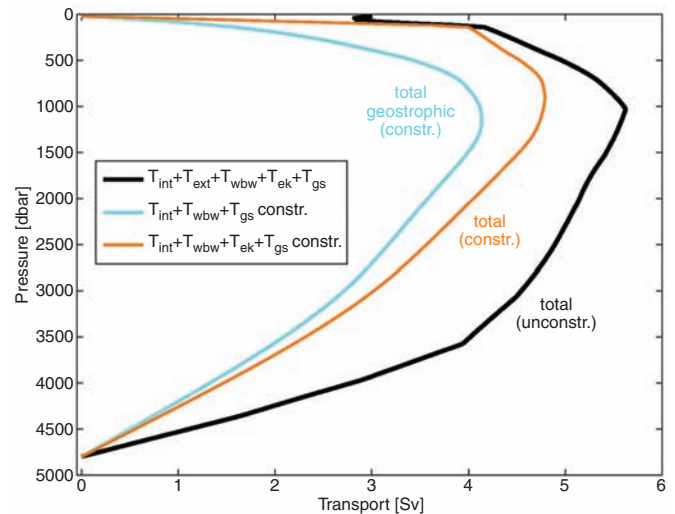


Fig. 4. MOC-transport fluctuations: cumulative-transport variability at 1000 dbar (integrated upward from 4820 dbar) for the three different cases displayed in Fig. 3.

constrained MOC transport does not account for). The presence of the MAR has not been accounted for in our calculations. Including moored-density and bottom-pressure measurements on both flanks of the MAR allows for the computation of $T_{MO}(z)$ below the MAR crest independently for the western and eastern basin (fig. S2). However, the effect of this on the temporal evolution of unconstrained MOC time series is rather small (fig. S3), with the difference between calculations taking into account and neglecting the measurements on the MAR flanks varying by ± 1.1 Sv (SOM).

Fluctuations in $\overline{T_{EK}}$ of ± 3.9 Sv do not dominate MOC variability on subseasonal time scales at 26.5°N. Rather, we observe an equal share of variability between Ekman and density contributions, with the constrained total geostrophic MOC solution (excluding $\overline{T_{EK}}$) displaying ± 4.1 Sv. We have presented evidence that the depth-independent compensation for $\overline{T_{EK}}$ is partly contained in $\overline{T_{EXT}}$. We have demonstrated the validity of our MOC-observing approach and described previously unobserved basic characteristics of the MOC variability near 26.5°N in the Atlantic after 1 year of continuous observations.

References and Notes

1. R. Dickson, J. Brown, *J. Geophys. Res.* **99**, 12319 (1994).
2. A. Ganachaud, C. Wunsch, *J. Clim.* **16**, 696 (2003).
3. M. Vellinga, R. A. Wood, *Clim. Change* **54**, 251 (2002).
4. S. Rahmstorf, *Nature* **421**, 699 (2003).
5. H. L. Bryden, H. R. Longworth, S. A. Cunningham, *Nature* **438**, 655 (2005).
6. J. J.-M. Hirschi, P. D. Killworth, J. R. Blundell, *J. Phys. Oceanogr.* **37**, 1246 (2007).
7. S. R. Jayne, J. Marotzke, *Rev. Geophys.* **39**, 385 (2001).
8. B. W. Dong, R. T. Sutton, *Geophys. Res. Lett.* **28**, 2445 (2001).
9. J. Marotzke, S. A. Cunningham, H. L. Bryden, *Monitoring the Atlantic Meridional Overturning Circulation at 26.5°N* (Southampton Oceanography Centre, Southampton, UK, 2002).
10. S. A. Cunningham, *RRS Discovery Cruise 277/278* (Report No. 53, National Oceanography Centre, Southampton, UK, 2004).
11. T. Kanzow, U. Send, W. Zenk, A. D. Chave, M. Rhein, *Deep-Sea Res.* **1** **53**, 528 (2006).
12. W. E. Johns, T. Kanzow, R. Zantopp, *Deep-Sea Res.* **1** **52**, 1542 (2005).
13. J. C. Larsen, T. B. Sanford, *Science* **227**, 302 (1985).
14. J. Graf *et al.*, *Acta Astronaut.* **43**, 397 (1998).
15. T. Whitworth III, *J. Phys. Oceanogr.* **13**, 2045 (1983).
16. S. A. Cunningham *et al.*, *Science* **317**, 935 (2007).
17. Estimates of variability and uncertainty refer to 1 SD.
18. $1 \text{ Sv} = 10^6 \text{ m}^3 \text{ s}^{-1}$.
19. Statistical significance is stated at a 5% error probability.
20. A. T. Roach *et al.*, *J. Geophys. Res.* **100**, 18443 (1995).
21. T. Kanzow *et al.*, *J. Geophys. Res.* **110**, C09001 (2005).
22. M. Hirose, I. Fukumori, R. M. Ponte, *Geophys. Res. Lett.* **28**, 2441 (2001).
23. W. Brown, W. Munk, F. Snodgrass, H. Mofjeld, B. Zetler, *J. Phys. Oceanogr.* **5**, 75 (1975).
24. C. S. Meinen, M. O. Baringer, S. L. Garzoli, *Geophys. Res. Lett.* **33**, L17610 (2006).
25. C. S. Meinen, *Deep-Sea Res.* **1** **48**, 1553 (2001).
26. We thank the captains and crews of the research vessels *Charles Darwin*, *Discovery*, *Ronald Brown*, and *Knorr* and the National Marine Facilities Sea Systems mooring team. The mooring operations have been funded by the Natural Environment Research Council, RAPID, and NSF. The Florida Current cable data are made freely available by the Atlantic Oceanographic and Meteorological Laboratory (www.aoml.noaa.gov/phod/floridacurrent/) and are funded by the NOAA Office of Climate Observations. The wind-stress data were obtained from Centre ERS d'Arquive et de Traitement the Institut Français de Recherche pour l'Exploration de la Mer in Plouzané, France.

Supporting Online Material

www.sciencemag.org/cgi/content/full/317/5840/938/DC1
Materials and Methods
SOM Text
Figs. S1 to S3
Tables S1 to S3
References

14 February 2007; accepted 12 July 2007
10.1126/science.1141293

Reduced Egg Investment Can Conceal Helper Effects in Cooperatively Breeding Birds

A. F. Russell,^{1,2*}† N. E. Langmore,³ A. Cockburn,^{3,4} L. B. Astheimer,⁵ R. M. Kilner^{6*}

Cooperative breeding systems are characterized by nonbreeding helpers that assist breeders in offspring care. However, the benefits to offspring of being fed by parents and helpers in cooperatively breeding birds can be difficult to detect. We offer experimental evidence that helper effects can be obscured by an undocumented maternal tactic. In superb fairy-wrens (*Malurus cyaneus*), mothers breeding in the presence of helpers lay smaller eggs of lower nutritional content that produce lighter chicks, as compared with those laying eggs in the absence of helpers. Helpers compensate fully for such reductions in investment and allow mothers to benefit through increased survival to the next breeding season. We suggest that failure to consider maternal egg-investment strategies can lead to underestimation of the force of selection acting on helping in avian cooperative breeders.

In cooperative breeding systems, offspring receive food from helpers in addition to their parents. Although parents can reduce the

rate at which they feed their offspring in the presence of helpers, this reduction is usually incomplete, and so offspring receive more food when helpers are present than when they are absent (1). Given that offspring receive more food when also provisioned by helpers, it is currently unclear why many long-term studies have failed to detect helper effects on offspring growth and survival (2) or have detected only weak effects (3). This failure to document the benefits to offspring has prompted hypotheses proposing that helping behavior is an unselected consequence of physiological priming to provide care to begging offspring (4), is contingent on future reciprocity (5), or is a form of “rent payment” (6). These alternatives are problematic because helping has been shown to be costly (7) and strategically

directed to maximize benefits (3, 8), cooperative breeding based on direct reciprocity is inherently unstable (9), and rent payment occurs under conditions that will be seldom met (10).

In cooperative breeding systems, securing and maintaining a breeding position is particularly challenging but offers substantial fitness benefits (11). Consequently, breeders might be expected to be under strong selection to reduce their investment in each reproductive attempt in order to increase the number of attempts that they can have in a lifetime. For example, one of the most commonly reported helper effects in avian cooperative breeding systems is load lightening, where breeding females reduce offspring provisioning with increasing helper numbers (1). Load lightening could also occur at the egg stage (12). However, despite growing evidence from noncooperative species that female birds can adaptively manipulate investment within eggs (13), this possibility has not been explored in cooperatively breeding species. Furthermore, hypotheses regarding such adaptive maternal egg investment typically predict that mothers should increase their level of within-egg investment when breeding in favorable conditions (14, 15). Yet it is also theoretically plausible that mothers breeding in privileged circumstances (in this case, with the benefit of helpers) might also benefit from reductions in egg investment, if the future fitness payoffs from doing so exceed the current fitness payoffs from increasing egg investment. If mothers reduce their investment in eggs when breeding in the presence of helpers, then any benefit that helpers might have on offspring condition and survival will be masked.

¹Department of Animal and Plant Sciences, University of Sheffield, Sheffield S10 2TN, UK. ²Centre for the Integrative Study of Animal Behaviour, Macquarie University, Sydney NSW 2109, Australia. ³School of Botany and Zoology, Australian National University, Canberra ACT 0200, Australia. ⁴Percy Fitzpatrick Institute of African Ornithology, Department of Science and Technology/National Research Foundation Centre of Excellence, University of Cape Town, Rondebosch 7701, South Africa. ⁵School of Health Sciences, University of Wollongong, Wollongong New South Wales 2522, Australia. ⁶Department of Zoology, University of Cambridge, Cambridge CB2 3EJ, UK.

*These authors contributed equally to this work.

†To whom correspondence should be addressed. E-mail: a.f.russell@sheffield.ac.uk